

Octopus-Inspired Smart Adhesive Pads for Transfer Printing of Semiconducting Nanomembranes

Hochan Lee, Doo-Seung Um, Youngsu Lee, Seongdong Lim, Hyung-jun Kim, and Hyunhyub Ko*

Smart adhesives with switchable adhesion on demand have potential applications in medical adhesives, industrial assembly and manipulation systems, and smart-printing systems. Nature provides impressive examples of nano- and microstructured systems with excellent adhesion properties, e.g., the amazing dry adhesion abilities of a gecko's foot,^[1,2] the wet adhesive capabilities of a mussel's byssal thread,^[3,4] and the feet of tree frogs^[5,6] and insects.^[7–10] In addition to strong adhesion abilities, most biological adhesive systems actively control and switch their adhesive strength for locomotion. For switchable adhesion, geckos employ the anisotropic directional adhesion properties of the hierarchical structures on their feet.^[1,2] Tree frogs^[6,11] and insects^[7–10] such as beetles and crickets climb foreign surfaces through the liquid-bridge-mediated adhesion based on the secretion of mucus on their feet. Inspired by these biological adhesion properties and their structures, many artificial adhesives based on gecko-inspired directional dry adhesives,^[12–15] mussel-,^[4,12,16] frog-,^[17] and insect-inspired^[18,19] wet adhesives have been reported. However, it is still a great challenge to mimic these switchable adhesive systems because most biological adhesion systems utilize inherent muscular actions or adhesive materials with complex structures to control their switchable adhesion properties on demand. Smart adhesive systems based on the active control of adhesion via external signals such as temperature,^[20,21] light,^[22] humidity,^[23] and electric current^[24] have also been reported. However, most of the previous artificial adhesive systems do not provide a high on/off adhesive strength ratio (i.e., the ratio of the adhesive strengths in the high-/low-adhesion states) with excellent switchability. In particular, reversible adhesion with a high on/off switching ratio in a wet environment has rarely been demonstrated^[14,23,25–28] (refer to Table S1 in the Supporting Information for the comparison of reversible adhesion properties).

Octopus suckers have an excellent switchable wet adhesion capability, which enables its arms to adhere to any foreign surface. An octopus utilizes muscle actuation in its suckers

to control the pressure inside the suckers and thus the pressure difference between the inside and outside of the suckers, resulting in the generation of a switchable on/off adhesive strength on foreign surfaces^[29–32] (the details of the adhering mechanism of octopus suckers have been described later in this paper). Through muscle actuation, the octopus easily controls the adhesion with a negligible preload. Although several adhesive systems mimicking the adhering mechanism of octopus suckers have been reported to realize their unique adhesion capability, the previous octopus-inspired adhesive systems require an external preload^[33,34] during the adhesion process or additional instruments such as suctioning systems^[35,36] and power sources^[37] to induce a negative pressure inside the suction cups. Switchable adhesion systems requiring a preload during the attaching/detaching processes are complicated and cannot be easily applied to grasp or transport soft surfaces or thin materials.

By mimicking the muscle actuation to control cavity-pressure-induced adhesion of octopus suckers, we demonstrate smart adhesive pads in which the thermoresponsive actuation of a hydrogel layer on elastomeric microcavity pads enables excellent switchable adhesion in response to a thermal stimulus. The smart adhesive pad exhibits an adhesive strength of 59.1 kPa and an adhesion switching ratio of ≈ 170 in response to temperature change between 22 and 35 °C for repeated cycles. Between 22 and 61 °C, the smart adhesive pad shows maximum adhesion switching ratio of ≈ 293 with maximized adhesive strength of ≈ 94 kPa. As a proof-of-concept application, the smart adhesive pads can be employed in the transfer printing of semiconductor micro- and nanomembranes onto arbitrary substrates to fabricate heterogeneously integrated semiconductor devices. The smart-printed InGaAs transistors on Si substrates exhibit an excellent field-effect mobility (maximum: ≈ 3000 cm² V⁻¹ s⁻¹, average: ≈ 2026 cm² V⁻¹ s⁻¹) and on/off current ratio (maximum: $\approx 5.3 \times 10^3$, average: $\approx 4 \times 10^3$), which are among the best for heterogeneous InGaAs transistors (Table S2, Supporting Information), demonstrating the high efficiency of our smart-printing technique.

Figure 1a,b shows a photograph and a magnified scanning electron microscopy (SEM) image of octopus suckers. The adhering mechanism of an octopus sucker to a target surface is schematically shown in Figure 1c. In this mechanism, suction adhesion is generated and retained by the contraction of radial and meridional muscles (denoted as R and M, respectively) and released by the contraction of circular muscles (denoted as C).^[30–32] Originally, the pressures inside and outside the sucker cavity are the same ($P_{\text{cavity}} = P_{\text{out}}$). By the contraction of the radial muscle, the wall of sucker becomes thinned, and the

H. Lee, D.-S. Um, Y. Lee, S. Lim, Prof. H. Ko
School of Energy and Chemical Engineering
Ulsan National Institute of Science
and Technology (UNIST)
Ulsan Metropolitan City 689–798, Republic of Korea
E-mail: hyunhko@unist.ac.kr

Dr. H.-j. Kim
Center for Spintronics
Korea Institute of Science and Technology (KIST)
Seoul 136–791, Republic of Korea



DOI: 10.1002/adma.201601407

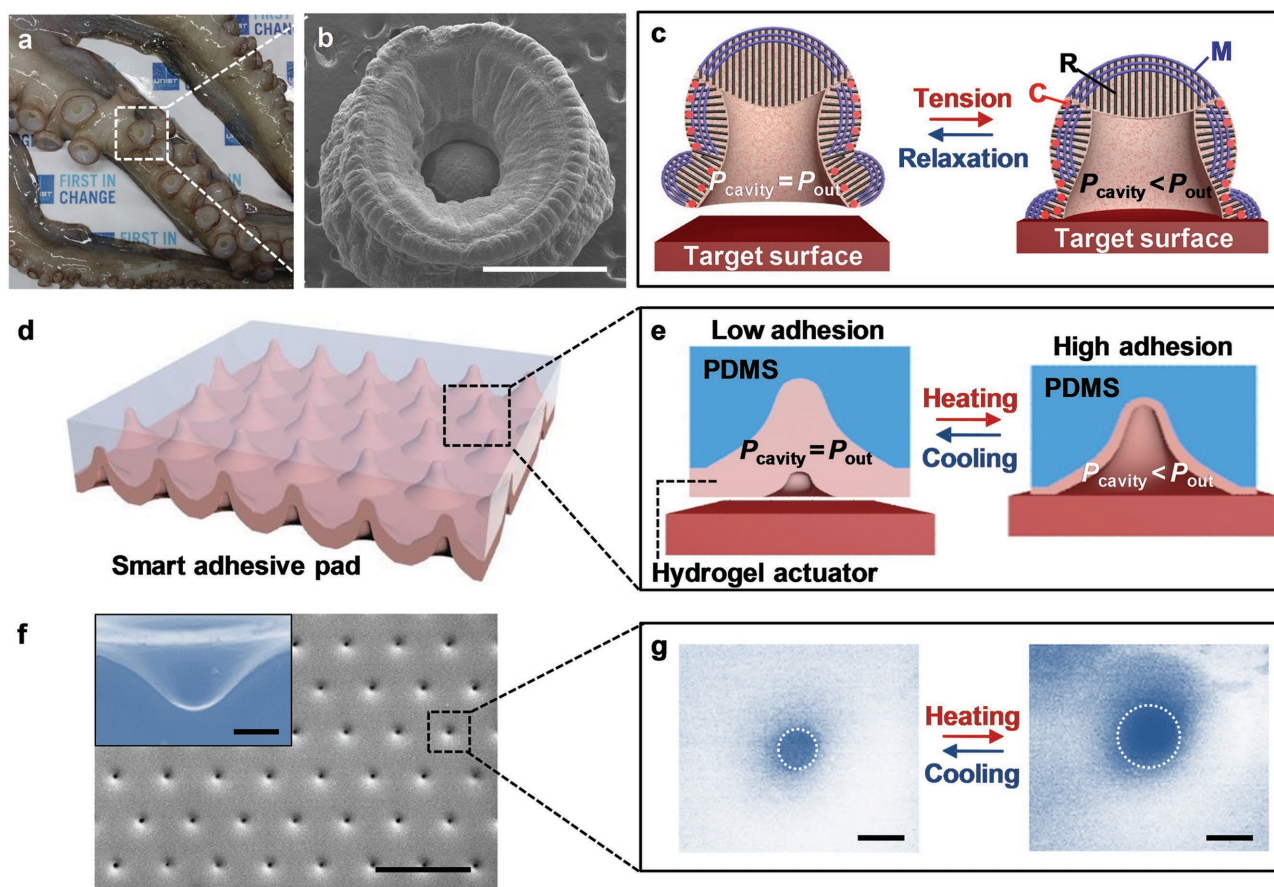


Figure 1. Octopus-inspired smart adhesive pad. a) A photograph of octopus tentacle with suckers and b) a magnified SEM image of an octopus sucker (scale bar: 1 mm). c) Schematic of the adhering process of an octopus sucker. The adhesion can be switched via the actuation of muscles (radial muscles, R; meridional muscles, M; circular muscles, C). d) Schematic representation of microcavity arrays within a smart adhesive pad. e) Schematic of switchable adhesion mechanism of a smart adhesive pad. The adhesive force is reversibly switched by the hydrogel actuation in response to the environmental temperature. f) SEM image of the surface of the smart adhesive pad (scale bar: 10 μm). Its cross-sectional image is shown in the inset (scale bar: 500 nm). g) ESEM images of a single hole on the smart adhesive pad at a low temperature (left, $T \approx 3\text{ }^\circ\text{C}$) and a high temperature (right, $T \approx 40\text{ }^\circ\text{C}$) (scale bar: 500 nm).

volume of the inside cavity expands, which results in a reduction in the pressure inside the sucker cavity ($P_{\text{cavity}} < P_{\text{out}}$); thus, suction adhesion is induced by the pressure difference. At this time, the contraction of meridional muscle enables to maintain the pressure difference and thus the consequent suction adhesion. To detach its suckers from the target surface, the circular muscles contract, and subsequently, the wall of sucker becomes thickened, which results in an increase in the cavity pressure up to the external pressure ($P_{\text{cavity}} = P_{\text{out}}$); thus, the suction adhesion is lowered.

Inspired by the octopus sucker's adhesive system, we fabricated a smart adhesive pad in which the adhesive strength can be actively controlled by the thermoresponsive actuation of a muscle-like hydrogel layer within the cavity array, thereby inducing a pressure difference between the inside and outside of the cavity. Figure 1d,e shows schematics of the structure and adhering mechanism of the smart adhesive pad. In this smart adhesive pad, a hole-patterned poly(dimethylsiloxane) (PDMS) film was utilized as an elastomeric support. A thermoresponsive hydrogel of poly(*N*-isopropylacrylamide) (pNIPAM) was coated on top of this support for the formation of a thermoresponsive

actuator wall inside the PDMS cavity. A detailed description of the fabrication of the smart adhesive pad is provided in the Experimental Section and shown in Figure S1 in the Supporting Information. The pNIPAM hydrogel undergoes a phase transition at a lower critical solution temperature (LCST) ($\approx 32\text{ }^\circ\text{C}$), which causes a sharp change in its volume.^[38,39] Although the pNIPAM hydrogel becomes hydrophilic and swells at a temperature below the LCST ($T < \text{LCST}$), it becomes hydrophobic and shrinks as the temperature is increased above the LCST ($T > \text{LCST}$). This unique property of pNIPAM enabled various smart systems with thermoresponsive actuations.^[39–43] In our smart adhesive pad, the coated pNIPAM wall layer functions as a thermoresponsive actuator to actively control the cavity volume within the smart adhesive pad, resembling the actuating muscle in an octopus sucker for the reversible adhesion activity.

As can be seen in Figure 1e, the pNIPAM hydrogel layer is deposited within the PDMS cavity; thus, the cavity volume can be increased or decreased via heating or cooling, resulting in a change in the cavity pressure. When the temperature becomes elevated after the smart adhesive pad contacts a target surface,

the volume of the pNIPAM-coated PDMS cavity is increased via shrinking of the hydrogel layer. Therefore, the cavity pressure decreases, which induces an adhesion force between the adhesive pad and the target surface through the pressure difference between the inside and outside of the cavity. When the adhesive pad is cooled, the opposite behavior (hydrogel swelling and a decrease in the cavity volume) induces a decrease in the pressure difference and thus the adhesive strength of the smart adhesive pad. All of these processes are reversible; thus, switchable adhesion can be achieved.

Figure 1f shows an SEM image of a smart adhesive pad containing a hexagonal hole array coated with a pNIPAM hydrogel layer. The cross-sectional geometry of a hole on the adhesive pad is shown in the inset in Figure 1f. As can be seen in the SEM images of PDMS hole arrays before and after coating with pNIPAM (Figure S2, Supporting Information), the pNIPAM layer uniformly coats the hole arrays with a thickness of $\approx 90 \pm 10$ nm. The pNIPAM coating on the hole-patterned PDMS is also confirmed via several analyses before and after coating with pNIPAM, including contact-angle measurements, attenuated total reflectance Fourier transform infrared (ATR FTIR) spectroscopy, and X-ray photoelectron spectroscopy (XPS) (Figure S3, Supporting Information). To investigate the thermoresponsive actuation of the pNIPAM hydrogel layer on the hole arrays, the change in the thickness of the pNIPAM layer at low (3 °C) and high (40 °C) temperatures was investigated by environmental SEM (ESEM). As shown in Figure 1g, it is observed that the diameter of the deep part of a hole increased from ≈ 420 to ≈ 670 nm (dotted circles), and the

size of the shallow part of a hole was also remarkably enlarged owing to shrinking of the pNIPAM layer after heating. The ESEM analysis indicates the change in the PDMS hole size at low and high temperatures, demonstrating the thermoresponsive actuation of the pNIPAM wall layer and supporting the suggested adhesion mechanism of our smart adhesive pad. Since the adhesion mechanism depends on the pressure difference and thus the volumetric change of holes on the smart adhesive pad, it is worthwhile to analyze the volumetric change of a hole when the temperature changes from 3 to 40 °C. For the calculation of volume change of a hole, we assumed the hole shape to be a conical frustum (Figure S4, Supporting Information). When the hole diameter changes from 420 to 670 nm, the hole volume changes from 2.75×10^8 to 10.25×10^8 nm³, which corresponds to $\approx 273\%$ change of a hole volume. This large change of a hole volume can result in the large pressure difference and thus the strong adhesion between the smart adhesive pad and the target surface. The large structural change of pNIPAM hydrogel has been similarly observed in several previous works due to swelling/shrinking behaviors.^[39–42,44]

The adhesive performance of a smart adhesive pad was investigated with a target surface of Si through a home-built adhesion tester (Figure S5, Supporting Information). As can be seen in Figure 2a, the pNIPAM-coated patterned PDMS (i.e., the smart adhesive pad) exhibits an adhesive strength (normal adhesion) of ≈ 46 kPa in a high-adhesion state (on state, $T \approx 35$ °C), which is over four times higher than the values observed for PDMS, patterned PDMS, and pNIPAM-coated PDMS. On the other hand, the adhesive strength of the smart

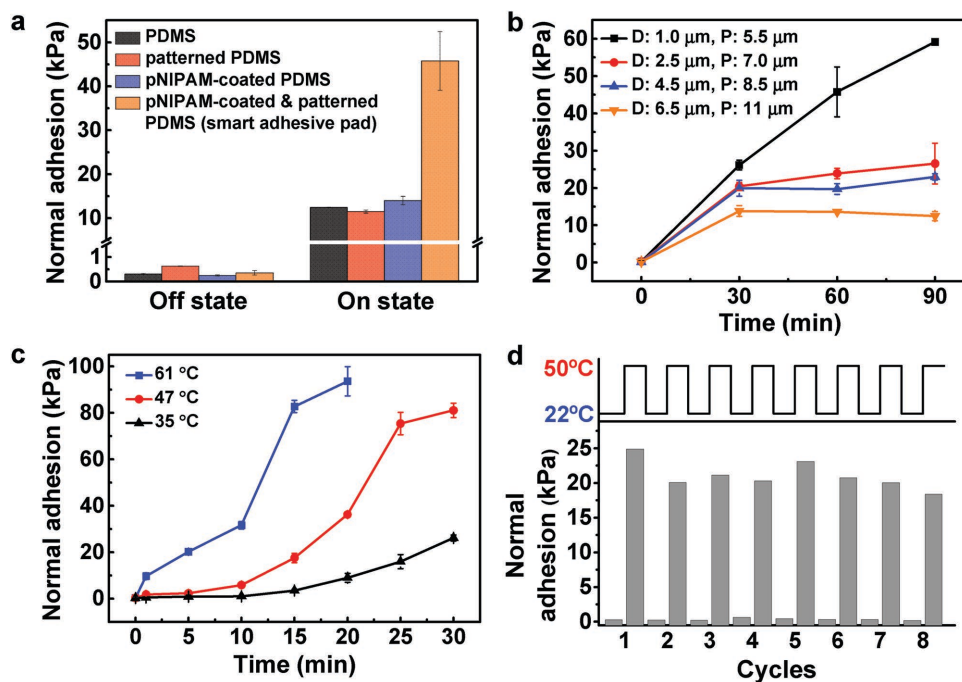


Figure 2. Adhesive performances of smart adhesive pads in response to the environmental temperature. a) Normal adhesive strength of various adhesive pads at 22 (adhesion off state) and 35 °C (adhesion on state). b) Normal adhesive strength of smart adhesive pads as a function of the attachment time at 35 °C for various diameters and pitches. c) Normal adhesive strength of a smart adhesive pad (diameter: 1.0 μm, pitch: 5.5 μm) as a function of the time of attachment at various heating temperatures (35, 47, 61 °C). d) Switchable normal adhesion of a smart adhesive pad (diameter: 1.0 μm, pitch: 5.5 μm) at a low temperature (22 °C) and a high temperature (35 °C). The attachment time is 30 min in both cases. For all the adhesion tests, the target surface is Si substrate and eight trials of adhesion test are performed to obtain the average adhesive strength.

adhesive pad in the low-adhesion state (off state, $T \approx 22$ °C, room temperature) is ≈ 0.3 kPa, which is comparable to those of other adhesives. This thermoresponsive change in the adhesive strength results in an on/off adhesive strength ratio which is greater than 131. The adhesion performance of the smart adhesive pads depends on the diameter and pitch of the hole arrays. As can be seen in Figure 2b, the adhesive strength increases as the diameter and pitch of the patterned holes becomes smaller. In the case of the smart adhesive pad with the smallest diameter and pitch (diameter: 1.0 μm , pitch: 5.5 μm), the adhesive strength in the high-adhesion state is ≈ 59.1 kPa for an attachment time of 90 min, and the obtained on/off ratio of the adhesive strength is ≈ 170 . The response time of smart adhesive system depends on the temperature. Figure 2c shows the time-dependent variation of adhesion strength of smart adhesive pads depending on various temperatures (35, 47, 61 °C). When the temperature is increased, the response time is shortened and the adhesive strength of smart adhesive pad is increased; the adhesive pads showed adhesive strengths of 9–26 kPa within 20–30 min of heating at 35 °C, 17–81 kPa within 15–30 min of heating at 47 °C, and 20–94 kPa within 5–20 min of heating at 61 °C. Figure 2b,c indicates that the adhesive strength and response time can be varied depending on the structure and temperature of smart adhesive pad. The maximum adhesive strength (≈ 94 kPa) and adhesion switching ratio (≈ 293) at 61 °C of heating temperature are significantly higher than those of previous smart adhesive pads^[14,23,25–28] (see the comparison in Table S1, Supporting Information). In particular, in contrast to previous smart adhesive pads, our smart adhesive pads do not require any external preload to enhance the adhesion state. Furthermore, the adhesive strength could be reversibly and repeatedly switched by active control of the temperature, as shown in Figure 2d, with repeated cycles of high and low temperatures. The smart adhesive pad shows a high durability as well. The smart adhesive pad maintained its performance, even after 100 repeated cycles of attachment/detachment processes with the target surface (Figure S6, Supporting Information).

One potential application of a smart adhesive pad with thermoresponsive reversible adhesion properties is the transfer printing of semiconductor thin films from the source substrates to different substrates. For example, the heterogeneous integration of III–V compound semiconductor nanomembranes onto arbitrary substrates (Si, glass, plastic) has enabled various III–V electronics (transistors, light-emitting diodes, solar cells, spintronics) on arbitrary substrates which is not possible with conventional semiconductor processes.^[45–55] However, most of the previous transfer-printing techniques rely on the use of kinetically controlled adhesion in planar^[56] or structured^[57,58] elastomeric stamps, which has been considered a big challenge for the transfer of delicate micro-/nanostructures owing to the low on/off ratio of the adhesive strengths of the transferring stamp, and require the application of an external preload which can cause damage to and cracks in the target materials. Consequently, a smart adhesive pad with a high on/off adhesion ratio and without an external preload will be required for more delicate attachment/detachment of ultrathin and thus fragile semiconducting membranes onto any desired substrate without any damage.

We developed a smart-printing process based on the bioinspired smart adhesive system for the transfer printing of

micro-/nanostructure arrays of a semiconducting material onto various substrates. As shown in Figure 3, square-patterned InGaAs nanomembranes (thickness: 100 nm) on InAlAs/InP donor substrates can be successfully transferred onto an SiO₂/Si substrate via smart-printing process. First, square-patterned InGaAs nanomembrane arrays on InAlAs/InP substrates were fabricated and then transferred to intermediate PDMS substrates through the selective wet etching of the InAlAs/InP substrates (Figure S7, Supporting Information). The square array of InGaAs nanomembranes was separated from the PDMS mediator by the smart adhesive pad in the high-adhesion state. The high-adhesion state could be created after the initially swollen adhesive pad touched the InGaAs/PDMS at a high temperature ($T_{\text{H}} \approx 35$ °C) for 60 min in the atmosphere. Then, PDMS was manually removed, and the InGaAs nanomembrane array was successfully transferred onto the smart adhesive pad. Then, the array was sequentially transferred onto an SiO₂/Si substrate in the low-adhesion state of the smart pad, which could be set by immersing the InGaAs nanomembrane array on a smart pad in deionized water at low temperature ($T_{\text{L}} \approx 22$ °C) for 30 min. This smart-printing process is shown in Figure 3a and described in the Experimental Section. We observed that the yield resulting from the smart printing of this square-patterned InGaAs nanomembrane array is almost 100% without any noticeable defect formation, as shown in Figure 3b and Figure S8a (Supporting Information), and this process is also applicable to other structures such as the nanoribbons shown in Figure S8b in the Supporting Information. An atomic force microscopy (AFM) analysis confirmed that there was no noticeable damage to the semiconducting nanomembrane array during the smart-printing process (Figure 3c and Figure S9, Supporting Information). Figure S9 (Supporting Information) shows that the surface roughness of the InGaAs nanomembrane was maintained after the smart-printing process. Here, the high roughness of the InGaAs nanomembrane on the smart adhesive pad is due to the strong suction of the InGaAs nanomembrane into the hole of the smart pad due to the pressure difference,^[59] which can be recovered to its original state after transferring the InGaAs nanomembrane onto the SiO₂/Si substrate. This complete restoration of the InGaAs nanomembrane indicates that the smart-printing process is applicable to the transfer printing of ultrathin nanomembranes without damage or ripples in the nanomembranes.

The smart-printing process is a generic technique which can be applied to various micro-/nanostructured arrays on arbitrary rigid and flexible substrates. For example, Si microribbon (thickness: 2 μm) and InGaAs nanoribbon (thickness: 100 nm) arrays were successfully transfer-printed onto SiO₂/Si substrates (Figure 4a,c). Furthermore, the cross-junction stacking of Si microribbon arrays and heterostructure arrays of Si/InGaAs micro/nanoribbons can be easily fabricated on SiO₂/Si substrates via repeated smart-printing processes (Figure 4b,d). These results of cross-stacked semiconducting micro-/nanoribbons are difficult to achieve with traditional transfer-printing techniques relying on the kinetic properties of the elastomeric stamp owing to the low van der Waals interactions between stacked nanoribbons with small contact-area formation. In addition, honeycomb-shaped Si micromembranes can be reversibly detached and transferred onto various rigid and flexible

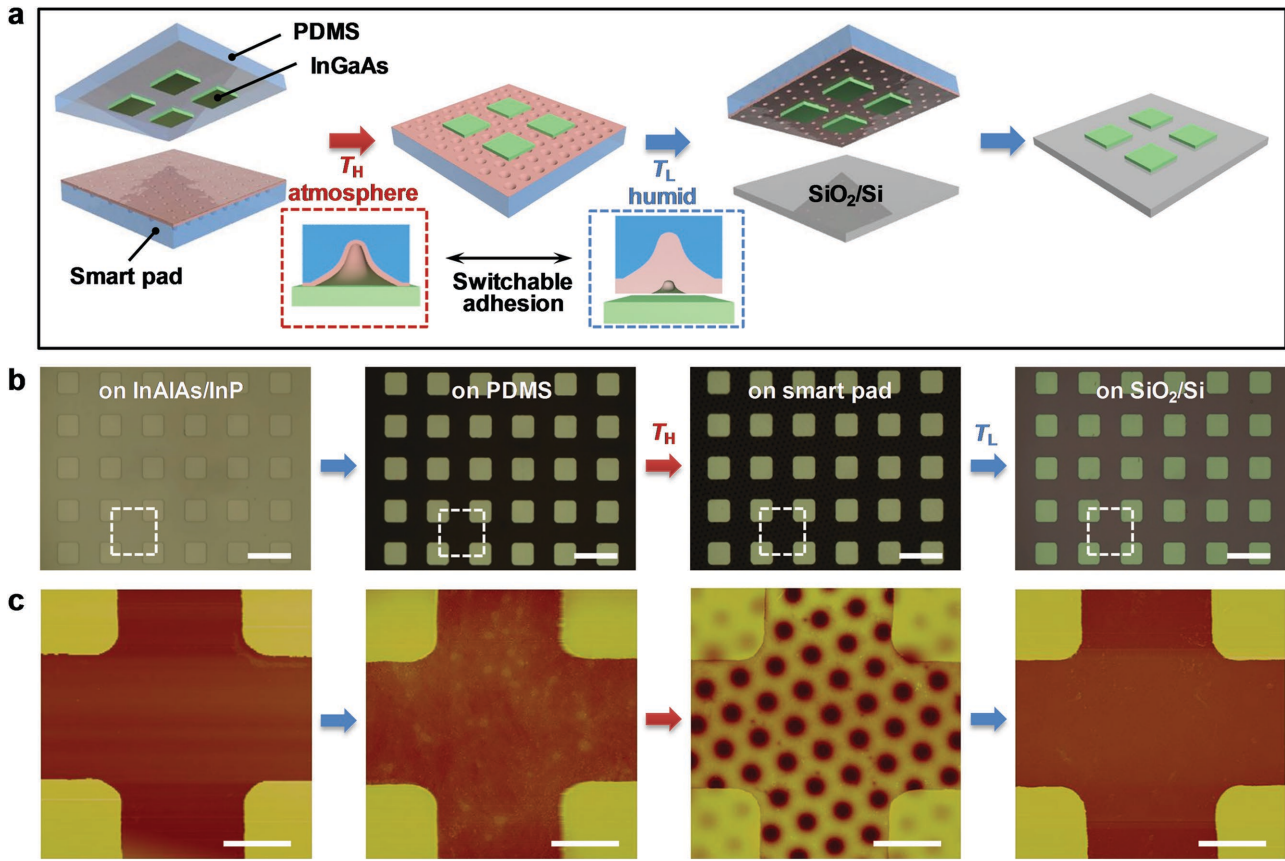


Figure 3. Smart printing of InGaAs nanomembranes on SiO_2/Si substrates. a) Schematic of the smart printing of a square-patterned InGaAs array onto a SiO_2/Si substrate. Square-patterned InGaAs nanomembranes were transferred onto a smart adhesive pad from a PDMS mediator in the high-adhesion state and sequentially transferred onto the SiO_2/Si substrate in the low-adhesion state. b) Optical microscope images (scale bar: $40\ \mu\text{m}$) and c) AFM images (scale bar: $10\ \mu\text{m}$) of the square-patterned InGaAs array on a series of substrates during wet etching and the subsequent smart-printing process; from left, square-patterned as-grown InGaAs array on an InAlAs/InP donor substrate, InGaAs on PDMS after selective wet etching of the donor substrates, InGaAs transferred onto a smart adhesive pad in the high-adhesion state, and InGaAs transferred onto SiO_2/Si substrates after the entire smart-printing process.

substrates such as an SiO_2/Si substrate, polyimide film, and thin poly(ethylene terephthalate) (PET) substrate without any damage (Figure 4e and Figure S10 in the Supporting Information). Here, it is worthwhile to note that identical Si micromembranes were sequentially detached at high temperature (T_H) and transferred at low temperature (T_L) to other substrates, demonstrating the high efficiency of the smart-printing process. In addition, this result also demonstrates that the hydrophobic material can be easily transferred by the smart-printing process. The Si micromembrane shows a hydrophobic property (Figure S11, Supporting Information) since the native oxide on the Si surface is removed by the hydrofluoric acid (HF) solution treatment during the preparation of honeycomb-shaped Si micromembrane. These results indicate that smart-printing technology using a smart adhesive pad is universal and versatile for the transfer of micro-/nanostructure arrays of various semiconducting materials onto any desired substrate.

Through the smart-printing technique, we fabricated heterogeneously integrated *n*-InGaAs nanomembrane transistors on an SiO_2/Si substrate. First, an array of InGaAs nanomembranes (thickness: $40\ \text{nm}$, length and width: $50\ \mu\text{m}$) was transferred onto an SiO_2/Si substrate (SiO_2 layer thickness of $100\ \text{nm}$) by

the smart-printing process. Then, Au source/drain electrodes were deposited via thermal evaporation. The device structure is schematically shown in Figure 5a (the inset shows an AFM image of the device), and an optical microscope image of the InGaAs nanomembrane transistor array is shown in Figure 5b. The heterointegrated InGaAs transistor exhibits a nice InGaAs/ SiO_2 interface without any voids or defects at the interface, as can be seen in the transmission electron microscopy (TEM) images (Figure 5c,d).

The transfer and output characteristics of a back-gated InGaAs field-effect transistor (FET) with a channel length of $35\ \mu\text{m}$ are shown in Figure 5e,f, respectively. The drain current increases as the gate voltage sweeps from negative to positive voltage, indicating the *n*-type behavior of the transistor (Figure 5e). The transistor exhibits a significantly high electron mobility and on/off current ratio. The field-effect mobility ($\mu_{n,\text{FE}}$) of our device was calculated by using the relation of $\mu_{n,\text{FE}} = g_m(L^2/C_{\text{OX}}V_{\text{DS}})$, where g_m is the transconductance, L is the channel length, C_{OX} is the gate oxide capacitance, and V_{DS} is the drain-source voltage. The transconductance (g_m) could be expressed by the relation of $g_m = dI_{\text{DS}}/dV_{\text{GS}}|_{V_{\text{DS}}}$, where I_{DS} is the drain-source current,

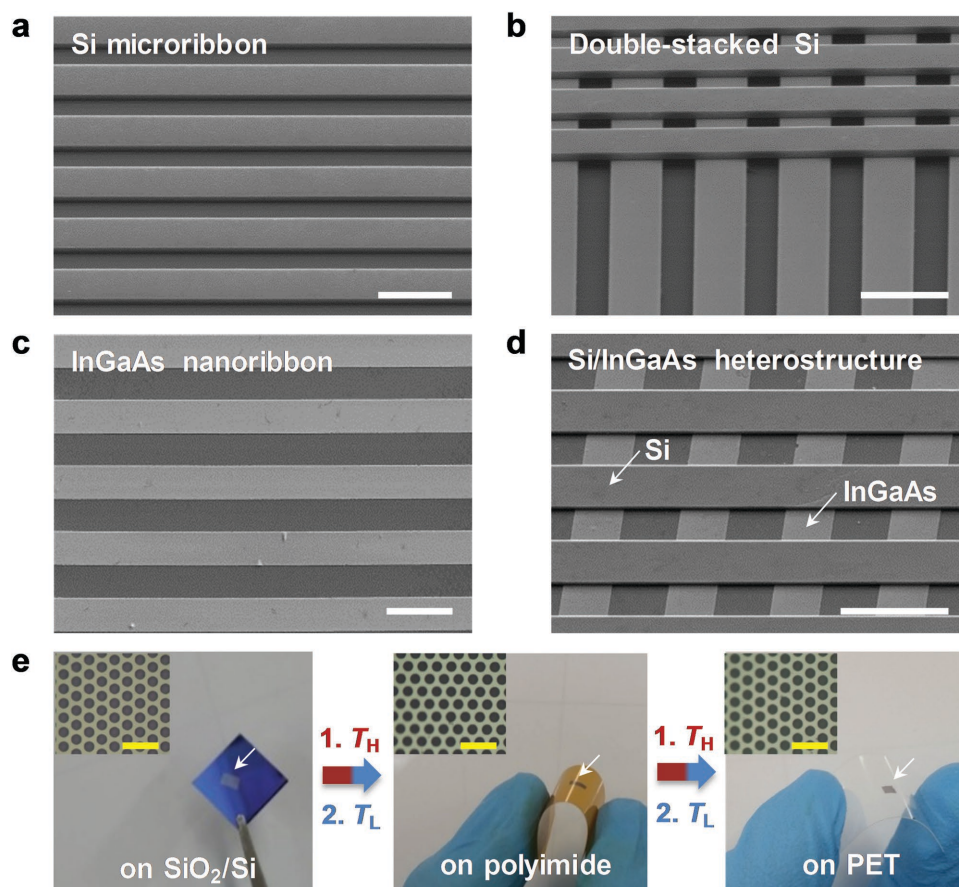


Figure 4. Smart printing of various semiconducting materials on diverse rigid and flexible substrates. Tilted SEM images of a smart-printed a) Si microribbon, b) cross-double-stacked Si microribbon, c) InGaAs nanoribbon, and d) cross-integrated heterostructure of Si/InGaAs on SiO₂/Si substrates. The thicknesses of each Si microribbon and InGaAs nanoribbon are 2 μm and 100 nm, respectively. The tilted angles are 60° in panels (a) and (b) and 45° in panels (c) and (d) (scale bar in panels (a) and (b): 20 μm and in panels (c) and (d): 40 μm). e) Photographs and optical microscope images (inset, scale bar: 30 μm) of a hexagonally patterned Si membrane sequentially transferred by smart printing onto SiO₂/Si, polyimide film, thin PET substrates, respectively (from left). The Si membrane can be detached from the original substrate at a high temperature (T_H) and transferred onto the other substrate at a low temperature (T_L). The thickness of the hexagonally patterned Si membrane is 2 μm.

V_{GS} is the gate–source voltage. The gate oxide capacitance (C_{OX}) could be expressed by the parallel plate capacitor model $C_{OX} = (\epsilon A)/d$, where $\epsilon = \epsilon_r \epsilon_0$ is the permittivity with relative permittivity $\epsilon_r = 3.9$ for SiO₂ dielectric layer, and d (in this case, $d = 100$ nm) is the thickness of dielectric layer. Figure 5g,h shows the histogram plots of the field-effect mobility and on/off ratio for 80 transistors. The maximum values of mobility and on/off current ratio are ≈ 3000 cm² V⁻¹ s⁻¹ and 5.3×10^3 (averages: ≈ 2026 cm² V⁻¹ s⁻¹ and 4×10^3), respectively. To the best of our knowledge, this mobility is the largest among heterogeneously integrated InGaAs FETs on Si substrates with top- or bottom-gate structures^[60–66] (see Table S2, Supporting Information). These results of high electron mobility and on/off current ratio indicate the excellent electronic quality of the transferred InGaAs layer and the efficiency of the transfer printing via the suggested octopus-inspired smart adhesive system.

By mimicking the pressure-induced adhesion of octopus suckers in this study, we demonstrated that the combination of the thermoresponsive actuation of a pNIPAM polymer layer and an elastomeric PDMS microcavity array enables switchable

adhesion in response to a thermal stimulus. Through control of the temperature, the smart adhesive pad showed an adhesion switching ratio of ≈ 293 , where the adhesive strength can be switched between ≈ 94 kPa at a high temperature and ≈ 0.32 kPa at a low temperature with clear reversibility and high durability. Furthermore, we showed that this switchable adhesive system can be employed in a transfer-printing process to heterogeneously integrate Si and compound semiconductor micro/nanomembranes onto any desired substrate such as Si, polyimide, and PET substrates. The smart-printed InGaAs transistors on Si substrates exhibited an excellent field-effect mobility (≈ 3000 cm² V⁻¹ s⁻¹) and on/off current ratio ($\approx 5.3 \times 10^3$), which are among the best for heterogeneous InGaAs transistors. The bioinspired smart adhesive system suggested in this study is applicable to the heterogeneous integration of arbitrary micro/nanoscale objects, which has great potential in the fabrication of high-performance transistors and optoelectronic devices on heterogeneous or flexible substrates. Moreover, our smart adhesive pads have potential applications in medical adhesives and assembly of micro- and macroscale objects in industrial manipulation systems.

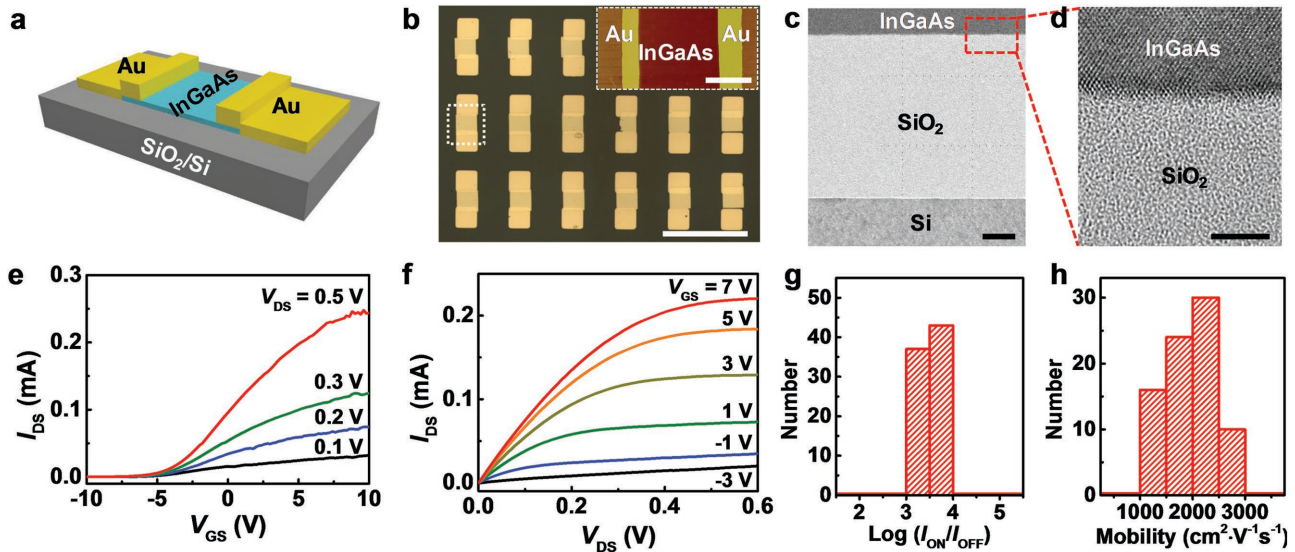


Figure 5. Heterogeneously integrated InGaAs FETs on SiO₂/Si substrates. a) Schematic representation and b) optical microscope image (scale bar: 200 μm) and AFM image (inset, scale bar: 20 μm) of *n*-InGaAs FETs on an SiO₂/Si substrate. c) Cross-sectional TEM image of an *n*-InGaAs back-gated FET (scale bar: 20 nm) and d) magnified TEM image of the InGaAs/SiO₂ interface (scale bar: 5 nm). e) V_{GS} - I_{DS} and f) V_{DS} - I_{DS} curves of *n*-InGaAs back-gated FETs on SiO₂/Si substrates. Histograms of the g) on/off ratio and h) field-effect mobility of *n*-InGaAs back-gated FETs on SiO₂/Si substrates.

Experimental Section

Fabrication of Smart Adhesive Pad: The fabrication process of smart adhesive pad was schematically shown in Figure S1 in the Supporting Information. First, patterned PDMS pad was fabricated. In this fabrication process, an Si mold was fabricated with four different diameters of 1.0, 2.5, 4.5, and 6.5 μm and pitches of 5.5, 7.0, 8.5, and 11 μm by photolithography and dry etching. Next, a thin film of parylene was deposited on the Si mold for the facile demolding of PDMS replica from the Si mold. For the PDMS replica moulding, a PDMS mixture (10:1 ratio for the PDMS base and curing agent, Sylgard 184, Dow Corning) was poured into the Si mold and degassed, followed by heating at 80 °C on a hot plate for 4 h. Then, PDMS was demolded from the Si mold, immersed in hexane for 2 h to remove the pre-polymer in the PDMS, and heated to evaporate the hexane at 70 °C for 2 h. Consequently, hole-patterned PDMS could be fabricated to be used as a smart pad supporter (Figure S12, Supporting Information).

Next, the pNIPAM hydrogel layer was deposited on patterned PDMS pad. Here, the pNIPAM layer was simultaneously synthesized and deposited onto the patterned PDMS by photopolymerization of a solution mixture containing an *N*-isopropylacrylamide (NIPAM) monomer, an *N,N'*-methylenebisacrylamide (bis-AMD) crosslinker, and a 2,2'-diethoxyacetophenone (DEAP) photoinitiator (Sigma Aldrich). The solution mixture was prepared by dissolving 1.6 mmol of NIPAM monomer, 30 μmol of bis-AMD, and 6 μmol of DEAP in 2 mL of deionized water and degassing the solution mixture with N₂ gas for 10 min to remove dissolved oxygen gas. The solution mixture was drop-cast onto patterned PDMS pad, which was treated with an O₂ plasma (18 W, for 2 min). Next, the solution was spread and softly squeezed by an O₂-plasma-treated (18 W, for 2 min) slide glass on top. Finally, photopolymerization was accomplished by UV irradiation for 2 h (365 nm, 6 W). Consequently, a thin layer of pNIPAM was coated onto patterned PDMS with a thickness of ≈90 nm.

Smart Printing of Patterned InGaAs Nanomembranes on SiO₂/Si Substrates: The smart-printing process was schematically described in Figure 3a and Figure S7 (Supporting Information). For the smart printing of InGaAs nanomembranes, *n*-In_{0.53}Ga_{0.47}As/In_{0.52}Al_{0.48}As epitaxial layers on InP (001) substrates were grown using a molecular beam epitaxy system (MBE) (Riber Compact 21T). The *n*-InGaAs layer was doped by $3.05 \times 10^{18} \text{ cm}^{-3}$ (at 440 °C), and it was covered by a 2 nm thick InAs capping layer to prevent surface oxidation at atmosphere. In

this process, In_{0.53}Ga_{0.47}As layers with a thickness of 100 nm (Figures 3 and 4, and Figure S8 in the Supporting Information) or 40 nm (Figure 5) were grown on an In_{0.52}Al_{0.48}As buffer layer (thickness ≈200 nm). Then, photoresist was deposited onto the In_{0.53}Ga_{0.47}As surface with a square (Figures 3 and 5, and Figure S8a in the Supporting Information) and line patterns (Figure 4, and Figure S8b in the Supporting Information) by photolithography. The unprotected area of In_{0.53}Ga_{0.47}As was etched by immersion (3 min) in an etching solution, which consisted of a 3:1 volumetric ratio of 50 wt% citric acid (citric acid monohydrate) (Sigma Aldrich) and hydrogen peroxide (34.5%, SAMCHUN, Korea). Then, the photoresist was removed by sonication in acetone for 10 min, resulting in square-patterned In_{0.53}Ga_{0.47}As layers on In_{0.52}Al_{0.48}As/InP substrates. Next, the substrate of In_{0.53}Ga_{0.47}As/In_{0.52}Al_{0.48}As/InP was washed with acetone, isopropyl alcohol (IPA), and deionized water.

Next, the In_{0.53}Ga_{0.47}As surface of the substrate was attached to the flat PDMS to pick up the In_{0.53}Ga_{0.47}As nanomembrane after the selective etching of In_{0.52}Al_{0.48}As/InP layers (Schematic description in Figure S7, Supporting Information). For the selective wet etching of In_{0.52}Al_{0.48}As/InP layers, the PDMS/In_{0.53}Ga_{0.47}As/In_{0.52}Al_{0.48}As/InP substrate was immersed (30 min at 40 °C) in an etching solution consisting of a 5:2 volumetric ratio of hydrochloric acid (35%, DAEJUNG, Korea) and deionized water. Then, the patterned In_{0.53}Ga_{0.47}As nanomembrane was remained on the flat PDMS pad. After washing the In_{0.53}Ga_{0.47}As nanomembrane on a PDMS pad with deionized water, In_{0.53}Ga_{0.47}As/PDMS was attached to a smart pad with a swollen pNIPAM hydrogel layer at a low-adhesion state (schematic description in Figure 3a). Then, the PDMS/In_{0.53}Ga_{0.47}As/smart pad was heated to 35 °C to shrink the pNIPAM hydrogel layer and thus switch the smart adhesion pad from low-adhesion to high-adhesion state. After 1 h, PDMS was delaminated by tweezers, and In_{0.53}Ga_{0.47}As was successfully transferred onto the smart pad. Then, the In_{0.53}Ga_{0.47}As/smart pad was immersed in deionized water for 30 min to swell the pNIPAM hydrogel layer and consequently switch the smart adhesive pad from the high-adhesion to low-adhesion state. Then, the In_{0.53}Ga_{0.47}As nanomembrane was successfully transferred onto an SiO₂/Si substrate via van der Waals interactions between In_{0.53}Ga_{0.47}As and SiO₂/Si substrates after the water layer on In_{0.53}Ga_{0.47}As was removed by an air blower.

Smart Printing of Patterned Si Membranes on Arbitrary Substrates: A silicon-on-insulator wafer containing an Si active layer (thickness: ≈2 μm) was utilized to prepare patterned Si membranes. Here, the photoresist was deposited onto the surface of the Si active layer with line or

hexagonal patterns by photolithography. Using a reactive-ion etching process, the line or hexagonal pattern was engraved into the Si active layer. Then, the photoresist was removed by sonication in acetone for 10 min, resulting in line- or hexagon-patterned Si membrane. Next, an SiO₂ sacrificial layer was etched with 4% HF for 9 h, resulting in a patterned Si active layer floated on the surface of etching solution. The floating membrane was picked up by another bare Si substrate, washed with IPA and deionized water, and dried with an N₂ blower. Then, the patterned Si membranes were transferred from the bare Si substrate onto the smart pad after contact for 1 h at 35 °C at the high-adhesion state of smart pad. Subsequently, the smart pad was swollen in room-temperature deionized water for 30 min to induce the low-adhesion state of smart pad, and the patterned Si membranes were transferred from the smart pad onto SiO₂/Si, PET, or polyimide substrates via contact printing.

Characterization: A field-emission SEM with the environmental mode (Quanta 200, FEI) was utilized for the precise monitoring of the smart pad at the swollen (3 °C, 50% humidity) and shrunken (40 °C, 9.8% humidity) states of pNIPAM hydrogel layer and thus the variation of diameter on the surface of the smart pad. The adhesive strength of an adhesive pad was investigated by a home-built adhesion tester containing a push–pull gauge (DFG10, OPTTECH) (Figure S5, Supporting Information). For the adhesion test, the adhesive pad was immersed in deionized water for 30 min for the stabilization of swollen state of an adhesive pad and the reproducibility of each adhesion test. Then, the adhesive pad was fixed to the load cell and attached on the target surface (Si substrate). Here, for the measurement of adhesive strengths at a high temperature, the hot plate was heated for 30 min before the adhesion test. After the contact of adhesive pad, the heat generated by the hot plate was transferred to the adhesive pad through a SUS (steel use stainless) plate and an Si substrate when the adhesive pad contacts with the Si substrate. To measure the adhesive strength at a low-adhesion state, the adhesive pad was immersed in a deionized water for 30 min at a low temperature and attached to the Si substrate. After a pre-defined attachment time, the adhesive pad was detached from the Si substrate and the adhesive strength was measured by the load cell. The surface morphology of In_{0.53}Ga_{0.47}As on the growth substrate, PDMS, smart pad, and SiO₂/Si substrate was examined by an optical microscope (PSM-1000, Olympus) and atomic force microscope (D3100, Veeco). The Si microribbon, InGaAs nanoribbon, cross-junction stacking of Si microribbon, and heterostructure arrays of Si/InGaAs micro/nanoribbon arrays transferred onto SiO₂/Si substrates were observed by a field-emission SEM (S-4800, Hitachi). The surface of the patterned PDMS before and after coating with pNIPAM was characterized by a field-emission SEM, contact-angle measurements, ATR FTIR spectroscopy (670/620-IR imaging, Agilent), and XPS (K-alpha, ThermoFisher) analyses.

Supporting Information

Supporting Information is available from the Wiley Online Library or from the author.

Acknowledgements

H.L. and D.-S.U. contributed equally to this work. This work was supported by the National Research Foundation of Korea (2015R1A2A1A10054152, 2011-0014965, 2015-004870), the Center for Advanced Soft-Electronics funded by the Ministry of Science, ICT and Future Planning as Global Frontier Project (2015M3A6A5065314), and the KIST Institutional Program.

Received: March 12, 2016

Revised: May 15, 2016

Published online:

- [1] K. Autumn, Y. A. Liang, S. T. Hsieh, W. Zesch, W. P. Chan, T. W. Kenny, R. Fearing, R. J. Full, *Nature* **2000**, *405*, 681.
- [2] Y. Tian, N. Pesika, H. B. Zeng, K. Rosenberg, B. X. Zhao, P. McGuiggan, K. Autumn, J. Israelachvili, *Proc. Natl. Acad. Sci. USA* **2006**, *103*, 19320.
- [3] H. Lee, N. F. Scherer, P. B. Messersmith, *Proc. Natl. Acad. Sci. USA* **2006**, *103*, 12999.
- [4] B. P. Lee, P. B. Messersmith, J. N. Israelachvili, J. H. Waite, *Annu. Rev. Mater. Res.* **2011**, *41*, 99.
- [5] G. Hanna, W. J. P. Barnes, *J. Exp. Biol.* **1991**, *155*, 103.
- [6] W. Federle, W. J. P. Barnes, W. Baumgartner, P. Drechsler, J. M. Smith, *J. R. Soc., Interface* **2006**, *3*, 689.
- [7] T. Eisner, D. J. Aneshansley, *Proc. Natl. Acad. Sci. USA* **2000**, *97*, 6568.
- [8] Y. Jiao, S. Gorb, M. Scherge, *J. Exp. Biol.* **2000**, *203*, 1887.
- [9] W. Federle, M. Riehle, A. S. G. Curtis, R. J. Full, *Integr. Comp. Biol.* **2002**, *42*, 1100.
- [10] J.-H. Dirks, W. Federle, *Soft Matter* **2011**, *7*, 11047.
- [11] W. J. P. Barnes, *MRS Bull.* **2007**, *32*, 479.
- [12] H. Lee, B. P. Lee, P. B. Messersmith, *Nature* **2007**, *448*, 338.
- [13] H. E. Jeong, J.-K. Lee, H. N. Kim, S. H. Moon, K. Y. Suh, *Proc. Natl. Acad. Sci. USA* **2009**, *106*, 5639.
- [14] M. P. Murphy, B. Aksak, M. Sitti, *Small* **2009**, *5*, 170.
- [15] Q. Xu, Y. Wan, T. S. Hu, T. X. Liu, D. Tao, P. H. Niewiarowski, Y. Tian, Y. Liu, L. Dai, Y. Yang, Z. Xia, *Nat. Commun.* **2015**, *6*, 8949.
- [16] B. K. Ahn, S. Das, R. Linstadt, Y. Kaufman, N. R. Martinez-Rodriguez, R. Mirshafian, E. Kesselman, Y. Talmon, B. H. Lipshutz, J. N. Israelachvili, J. H. Waite, *Nat. Commun.* **2015**, *6*, 8663.
- [17] D. M. Drotlef, L. Stepien, M. Kappl, W. J. P. Barnes, H. J. Butt, A. del Campo, *Adv. Funct. Mater.* **2013**, *23*, 1137.
- [18] M. J. Vogel, P. H. Steen, *Proc. Natl. Acad. Sci. USA* **2010**, *107*, 3377.
- [19] L. Xue, A. Kovalev, A. Eichler-Volf, M. Steinhart, S. N. Gorb, *Nat. Commun.* **2015**, *6*, 6621.
- [20] S. Khongtong, G. S. Ferguson, *J. Am. Chem. Soc.* **2002**, *124*, 7254.
- [21] Y. Xue, Y. Zhang, X. Feng, S. Kim, J. A. Rogers, Y. Huang, *J. Mech. Phys. Solids* **2015**, *77*, 27.
- [22] C. Heinzmann, S. Coulibaly, A. Roulin, G. L. Fiore, C. Weder, *ACS Appl. Mater. Interfaces* **2014**, *6*, 4713.
- [23] L. Xue, A. Kovalev, K. Dening, A. Eichler-Volf, H. Eickmeier, M. Haase, D. Enke, M. Steinhart, S. N. Gorb, *Nano Lett.* **2013**, *13*, 5541.
- [24] J. Eisenhaure, S. Kim, *Polymers* **2014**, *6*, 2274.
- [25] W.-G. Bae, D. Kim, K.-Y. Suh, *Nanoscale* **2013**, *5*, 11876.
- [26] K. Jin, J. C. Cremaldi, J. S. Erickson, Y. Tian, J. N. Israelachvili, N. S. Pesika, *Adv. Funct. Mater.* **2014**, *24*, 574.
- [27] S. Seo, J. Lee, K.-S. Kim, K. H. Ko, J. H. Lee, J. Lee, *ACS Appl. Mater. Interfaces* **2014**, *6*, 1345.
- [28] B. Yoo, S. Cho, S. Seo, J. Lee, *ACS Appl. Mater. Interfaces* **2014**, *6*, 19247.
- [29] A. M. Smith, *J. Exp. Biol.* **1991**, *157*, 257.
- [30] W. M. Kier, A. M. Smith, *Integr. Comp. Biol.* **2002**, *42*, 1146.
- [31] F. Tramacere, L. Beccai, M. Kuba, A. Gozzi, A. Bifone, B. Mazzolai, *PLoS One* **2013**, *8*, e65074.
- [32] F. Tramacere, N. M. Pugno, M. J. Kuba, B. Mazzolai, *Interface Focus* **2015**, *5*, 20140050.
- [33] W.-Y. Chang, Y. Wu, Y.-C. Chung, *Nano Lett.* **2014**, *14*, 1546.
- [34] M. K. Choi, O. K. Park, C. Choi, S. Qiao, R. Ghaffari, J. Kim, D. J. Lee, M. Kim, W. Hyun, S. J. Kim, H. J. Hwang, S.-H. Kwon, T. Hyeon, N. Lu, D.-H. Kim, *Adv. Healthcare Mater.* **2016**, *5*, 80.
- [35] F. Tramacere, L. Beccai, F. Mattioli, E. Sinibaldi, B. Mazzolai, in *2012 IEEE International Conference on Robotics and Automation (ICRA)*, IEEE, Piscataway, NJ, USA **2012**, p. 3846, DOI: 10.1109/ICRA.2012.6225058.
- [36] T. Tomokazu, S. Kikuchi, M. Suzuki, S. Aoyagi, in *2015 IEEE/RSJ International Conference on Intelligent Robots and Systems*

- (IROS), IEEE, Piscataway, NJ, USA **2015**, p. 2929, DOI: 10.1109/IROS.2015.7353781.
- [37] M. Follador, F. Tramacere, B. Mazzolai, *Bioinspiration Biomimetics* **2014**, *9*, 046002.
- [38] H. Yim, M. S. Kent, S. Mendez, S. S. Balamurugan, S. Balamurugan, G. P. Lopez, S. Satija, *Macromolecules* **2004**, *37*, 1994.
- [39] H. Ko, Z. Zhang, Y.-L. Chueh, E. Saiz, A. Javey, *Angew. Chem. Int. Ed.* **2010**, *49*, 616.
- [40] M. E. Harmon, M. Tang, C. W. Frank, *Polymer* **2003**, *44*, 4547.
- [41] J. Wang, Z. Chen, M. Mauk, K.-S. Hong, M. Li, S. Yang, H. H. Bau, *Biomed. Microdevices* **2005**, *7*, 313.
- [42] L. Dong, A. K. Agarwal, D. J. Beebe, H. Jiang, *Adv. Mater.* **2007**, *19*, 401.
- [43] R. Luo, J. Wu, N.-D. Dinh, C.-H. Chen, *Adv. Funct. Mater.* **2015**, *25*, 7272.
- [44] J. Yoon, S. Cai, Z. Suo, R. C. Hayward, *Soft Matter* **2010**, *6*, 6004.
- [45] J.-H. Ahn, H.-S. Kim, K. J. Lee, S. Jeon, S. J. Kang, Y. Sun, R. G. Nuzzo, J. A. Rogers, *Science* **2006**, *314*, 1754.
- [46] Y. Sun, J. A. Rogers, *Adv. Mater.* **2007**, *19*, 1897.
- [47] S.-I. Park, Y. Xiong, R.-H. Kim, P. Elvikis, M. Meitl, D.-H. Kim, J. Wu, J. Yoon, C.-J. Yu, Z. Liu, Y. Huang, K.-C. Hwang, P. Ferreira, X. Li, K. Choquette, J. A. Rogers, *Science* **2009**, *325*, 977.
- [48] H. Ko, K. Takei, R. Kapadia, S. Chuang, H. Fang, P. W. Leu, K. Ganapathi, E. Plis, H. S. Kim, S.-Y. Chen, M. Madsen, A. C. Ford, Y.-L. Chueh, S. Krishna, S. Salahuddin, A. Javey, *Nature* **2010**, *468*, 286.
- [49] J. A. del Alamo, *Nature* **2011**, *479*, 317.
- [50] M. Madsen, K. Takei, R. Kapadia, H. Fang, H. Ko, T. Takahashi, A. C. Ford, M. H. Lee, A. Javey, *Adv. Mater.* **2011**, *23*, 3115.
- [51] J. A. Rogers, M. G. Lagally, R. G. Nuzzo, *Nature* **2011**, *477*, 45.
- [52] A. Carlson, A. M. Bowen, Y. Huang, R. G. Nuzzo, J. A. Rogers, *Adv. Mater.* **2012**, *24*, 5284.
- [53] J. Nah, H. Fang, C. Wang, K. Takei, M. H. Lee, E. Plis, S. Krishna, A. Javey, *Nano Lett.* **2012**, *12*, 3592.
- [54] C. Wang, J.-C. Chien, H. Fang, K. Takei, J. Nah, E. Plis, S. Krishna, A. M. Niknejad, A. Javey, *Nano Lett.* **2012**, *12*, 4140.
- [55] K.-H. Kim, D.-S. Um, H. Lee, S. Lim, J. Chang, H. C. Koo, M.-W. Oh, H. Ko, H.-j. Kim, *ACS Nano* **2013**, *7*, 9106.
- [56] M. A. Meitl, Z.-T. Zhu, V. Kumar, K. J. Lee, X. Feng, Y. Y. Huang, I. Adesida, R. G. Nuzzo, J. A. Rogers, *Nat. Mater.* **2006**, *5*, 33.
- [57] S. Kim, J. Wu, A. Carlson, S. H. Jin, A. Kovalsky, P. Glass, Z. Liu, N. Ahmed, S. L. Elgan, W. Chen, P. M. Ferreira, M. Sitti, Y. Huang, J. A. Rogers, *Proc. Natl. Acad. Sci. USA* **2010**, *107*, 17095.
- [58] S. Kim, A. Carlson, H. Cheng, S. Lee, J.-K. Park, Y. Huang, J. A. Rogers, *Appl. Phys. Lett.* **2012**, *100*, 171909.
- [59] D.-S. Um, S. Lim, Y. Lee, H. Lee, H.-j. Kim, W.-C. Yen, Y.-L. Chueh, H. Ko, *ACS Nano* **2014**, *8*, 3080.
- [60] J. Noborisaka, T. Sato, J. Motohisa, S. Hara, K. Tomioka, T. Fukui, *Jpn. J. Appl. Phys.* **2007**, *46*, 7562.
- [61] Y. Xuan, Y. Wu, P. Ye, *IEEE Electron Device Lett.* **2008**, *29*, 294.
- [62] M. Yokoyama, T. Yasuda, H. Takagi, H. Yamada, N. Fukuhara, M. Hata, M. Sugiyama, Y. Nakano, M. Takenaka, S. Takagi, *Appl. Phys. Express* **2009**, *2*, 124501.
- [63] M. Yokoyama, T. Yasuda, H. Takagi, H. Yamada, Y. Urabe, N. Fukuhara, M. Hata, M. Sugiyama, Y. Nakano, M. Takenaka, S. Takagi, *ECS Trans.* **2010**, *33*, 391.
- [64] M. Yokoyama, R. Iida, S. Kim, N. Taoka, Y. Urabe, H. Takagi, T. Yasuda, H. Yamada, N. Fukuhara, M. Hata, M. Sugiyama, Y. Nakano, M. Takenaka, S. Takagi, *IEEE Electron Device Lett.* **2011**, *32*, 1218.
- [65] M. Yokoyama, H. Takagi, T. Yasuda, H. Yamada, N. Fukuhara, M. Hata, M. Sugiyama, Y. Nakano, M. Takenaka, S. Takagi, *Appl. Phys. Express* **2011**, *4*, 054202.
- [66] S. H. Kim, D.-M. Geum, M.-S. Park, W. J. Choi, *IEEE Electron Device Lett.* **2015**, *36*, 451.